Materials & Design 227 (2023) 111811

Contents lists available at ScienceDirect

Materials & Design

journal homepage: www.elsevier.com/locate/matdes

Thermal shape morphing of membrane-type electronics based on plastic-elastomer frameworks for 3D electronics with various Gaussian curvatures

Jung Il Yoo [a,1], Dukkyu Park [a,1], Seung Hyun Kim [a], Seonggwang Yoo [b], Hun Soo Jang [c,*], Jongwon Yoon [d,*], Heung Cho Ko [a,*]

[a] School of Materials Science and Engineering, Gwangju Institute of Science and Technology 123 Cheomdan-gwagiro, Buk-Gu, Gwangju 61005, Republic of Korea
[b] Querrey Simpson Institute for Bioelectronics, Northwestern University, Evanston, IL 60208, USA
[c] Materials Digitalization Center, Korea Institute of Ceramic Engineering and Technology, 101 Soho-ro, Jinju-si, Gyeongsangnam-do, 52851, Republic of Korea
[d] Department of Energy & Electronic Materials, Surface & Nano Materials Division, Korea Institute of Materials Science, 797 Changwon-daero, Sungsan-gu, Changwon-si, Gyeongsangnam-do 51508, Republic of Korea

HIGHLIGHTS

- Supportive frameworks consist of an elastomer film and shrinkable plastic lines inside with reliable interfacial adhesion of the heterogeneous materials.
- Morphing to various Gaussian curvatures is possible through thermal relaxation of plastic and biaxial deformation of the elastomer.
- Plastic-elastomer frameworks provide a platform technology for mounting and transforming membrane-type devices.

GRAPHICAL ABSTRACT

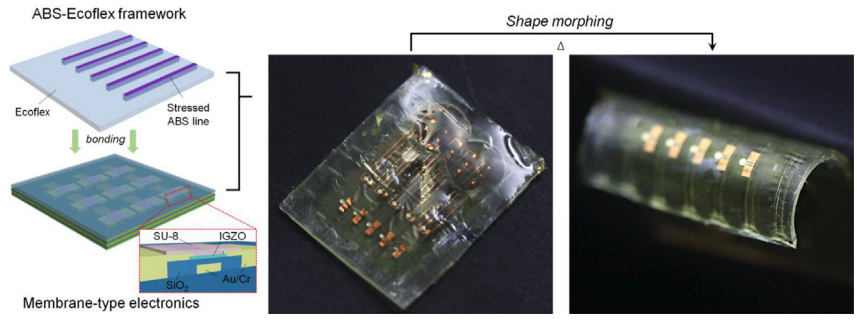

ARTICLE INFO

Article history:
Received 15 December 2022
Revised 15 February 2023
Accepted 5 March 2023
Available online 6 March 2023

Keywords:
3D electronics
Shape morphing
Plastic-elastomer framework
Flexible electronics
Interfacial adhesion

ABSTRACT

This study demonstrates a means of shape morphing planar membrane-type electronic devices into three-dimensional (3D) structures with various Gaussian curvatures using a plastic-elastomer supportive framework consisting of acrylonitrile–butadienestyrene (ABS) lines with tensile stress inside an Ecoflex film. The plastic part, created by extrusion shear printing (ESP), provides the driving force for shape morphing upon thermal annealing, whereas the elastomer part provides a base to mount membrane-type electronic devices and allows a comparably large degree of deformation. To ensure reliable interfacial adhesion in the plastic-elastomer framework, the ABS lines are treated with an allyl-terminated self-assembled monolayer (SAM) for chemical bonding to the Ecoflex layer. To determine control parameters for reliable shape morphing, the annealing conditions (e.g., temperature and time), the printing conditions (e.g., shear rate and pitch), and relative thicknesses of the ABS/Ecoflex are examined. Based on these findings, various 3D structures, including bent, cone, saddle, and dome shapes, can be generated from planar forms using ABS-Ecoflex frameworks, which are also predicted by a mechanical finite element method (FEM) simulation. Furthermore, a metal electrode and a membrane-type indium gallium zinc oxide (IGZO) transistor array are successfully mounted on ABS-Ecoflex frameworks and transformed into curvilinear structures without electrical failure.

* Corresponding authors.
E-mail addresses: hsjang@kicet.re.kr (H.S. Jang), jwyoon@kims.re.kr (J. Yoon), heungcho@gist.ac.kr (H.C. Ko).
[1] These two authors contributed equally to this work.

https://doi.org/10.1016/j.matdes.2023.111811
0264-1275/

1. Introduction

Many researchers have made tremendous efforts to develop three-dimensional (3D) image sensors [1–7], light-emitting devices [8], batteries [9,10], solar cells [11], and antennas [12,13] for detection, display, energy supply, and communication with minimized optical aberration and signal loss. When device fabrication on, for example, a curvilinear or polyhedral surface is too complicated or intrinsically impossible due to the nonplanar geometric structure, separately fabricating a membrane-type flexible electronic device and directly transferring it onto a target surface (e.g., a hemispherical surface [14], skin [15], and an organ [16]) or a supportive framework, actuatable by surface tension [17], residual stress [18–21], a magnetic field [22,23], light [24,25], prestrain [26–30] or mass transfer [31,32] to morph the overall shape into the desired structure, is highly desirable. This indirect method provides the substantial advantage of a broad selection range for electronic components and fabrication processes due to the use of base platforms to fabricate devices separate from target surfaces. Nevertheless, shape-morphing technology based on a supportive framework should involve the following concerns.

First, the device layer must be highly flexible. When the use of electronic devices with inorganic materials (e.g., Si, indium gallium zinc oxide (IGZO), SiO_2, and Au with ultimate strengths of 6.4, 0.2, 0.2, and 0.5 GPa) [33,34] accounts for the deformation strategy, the device layer should be fabricated as thin as possible (total thickness including the bottom substrate and top encapsulation layer = several micrometers), and the electrical components should be placed within the mechanical neutral plane [35]. Furthermore, the design of the device layer may employ pop-up structures [1], stretchable serpentine interconnects [5], origami designs [7], and placement of fragile components in relatively less strained zones [30] to accommodate an extensive strain range.

Second, a supportive framework affords a 2D to 3D geometric change without causing too much stress to the device layer. For example, shape morphing into a curvilinear structure with zero Gaussian curvature (a helix [20,25], a cylinder [33], and a gripper [18,23]) is possible through uniaxial bending and twisting with a plastic framework without crack formation. Plasticization with a solvent or heat affords deformation to a high degree of curvature (e.g., $\sim 1\ mm^{-1}$) owing to the viscoplastic behavior of the plasticized region; this strategy is beneficial for image sensors and display systems that require placing the device layer on the top surface of the framework (in other words, outside of a neutral mechanical plane) [2,8]. However, plastic alone has difficulty in achieving biaxial deformation due to the much smaller available elongation range and significant directional interference in biaxial deformation of a planar film structure [36], in particular limiting the shape morphing into a nonzero Gaussian curvature (e.g., a flower [20,37], a saddle [38], and a hemisphere [1,5,30]). Regarding the material candidates for the framework accommodating such complex deformation, employing elastomers with low moduli (e.g., polydimethylsiloxane (PDMS) and Ecoflex with Young's moduli of 1.3 ∼ 3.0 MPa and 0.1 ∼ 0.5 MPa) [39–41] and high elongation at break (e.g., ∼100% and ∼ 900% for PDMS and Ecoflex) in a supportive framework would be desirable, but guaranteeing reliable interfacial adhesion between heterogeneous materials is still a challenging issue.

In this study, we envisioned that introducing a plastic-elastomer supportive framework would prevent overlap of induced deformation stress and achieve various Gaussian curvatures. To achieve reliable interfacial adhesion between the plastic and elastomer layers, we performed a surface modification process with a self-assembled monolayer (SAM) on the plastic layer that can undergo chemical bonding to the upper elastic layer. Furthermore, to allow an automatic shape morphing capability, we used extrusion shear printing (ESP) as a conventional 3D printing method to provide stressed plastic lines that are shrinkable upon thermal relaxation. Our goal is to establish a rational design rule to guide the shape morphing of plastic-elastomer frameworks with manipulated plastic structures from simple stressed lines to more complex 2D and 3D meshes. In the acrylonitrile–butadienestyrene (ABS)-Ecoflex framework, where stressed ABS lines act as a deformation backbone with residual stress, Ecoflex serves as a skin that provides a large surface area for further electronic applications. To demonstrate the feasibility of this method, we successfully assembled ABS-Ecoflex frameworks and membrane-type electronics, such as a metal electrode and an IGZO transistor array, and successfully transformed them into complex 3D structures without electric failure.

2. Experimental methods

2.1. Fabrication of plastic-elastomer frameworks

ABS (PLASIL, source material: LG Chem, ABS HI121H) lines are printed using a 3D printer (LUGO, Former's Farm). The surface of ABS is treated with atmospheric surface plasma (plasma treatment, Plasmalife, 396 W, 20 s). Then, the sample is drop-cast with 2 vol% allyltrimethoxysilane (ATMS) (Tokyo Chemical Industry Co.) in DI water for 1 h and rinsed with DI water. Next, the sample is drop-cast with Sylgard 184B (Dow Corning) for 2 h and rinsed with *n*-hexane (DAEJUNG CHEMICALS & METALS CO. LTD.) and DI water. After a PET film, double-sided tape, and water-soluble tape (ASWT-2, Aquasol) are stacked in sequence on a bar coater plate, the modified-ABS film is placed, coated with the Ecoflex mixture (part a:b by weight = 1:1) using a bar coater and cured at 50 °C for 3 h to generate a plastic-elastomer framework. After the curing process is finished, the top plastic-elastomer framework layer is delaminated from the supportive PET film by dipping the sample in water to remove the water-soluble tape. For the case of the bare ABS film, the Ecoflex coating and retrieval processes are identical to the method mentioned above.

2.2. Fabrication of a membrane-type electrode

The fabrication begins with cleaning of a Si wafer chip (TAEWON SCIENTIFIC CO., LTD.) using acetone, isopropyl alcohol (IPA), and DI water under sonication. The cleaned Si chip is then dried with N_2 gas and deposited with a sacrificial layer (300-nm-thick GeO_x) using an RF magnetron sputtering system (KOREA VACUUM TECH., LTD, Ar/O_2 = 10/5, 2.5 mTorr, 60 W) and a buffer layer (100-nm-thick SiO_2) using plasma-enhanced chemical vapor deposition (PECVD, SNTECH Co. Ltd., $Ar/N_2O/SiH_4$ = 100/35/15 sccm, 270 °C, 2 Torr, 100 W). Then, spin coating of a poly(pyromellitic dianhydride-*co*-4,4′-oxydianiline) amic solution (Sigma-Aldrich) using a spin coater (MIDAS SYSTEM, 4000 rpm, 60 s) and a curing process on a hotplate at 250 °C for 2 h forms a 1.4-μm-thick PI film. Then, the PI film is coated with an additional 100-nm-thick SiO_2 buffer layer using PECVD (same conditions as above) to finalize the preparation of the printable substrate. After 10-nm-thick Cr and 90-nm-thick Au layers are formed on the printable substrate using a sputter, the metal lines are defined by patterning with a photoresist (PR) mask (mask aligner: CA-6 M, SHINU MST, 8.5 mW cm^{-1}; PR: AZ GXR-601, Merck, 3000 rpm, 35 s, exposure

time: 9 s; developer: AZ 500 MIF, Merck, 25 s) and wet etching of the metals using a Au etchant (GOLD ETCHANT TFA, TRANSENE COMPANY, INC.) and a Cr etchant (CR-7, KMG Electronic Chemicals, Inc.), followed by a cleaning process with acetone, an IPA rinse, and blow-drying. Additional 1.4-μm-thick PI and 100-nm-thick SiO_2 layers are formed using the previously explained coating and deposition process to encapsulate the electrode (in this case, the curing process of the PI film is performed at 150 °C for 3 h). Finally, the contact pad opening process for external connection is carried out using a dry etching process for the PI (O_2 = 20 sccm, 100 mTorr, 150 W, 7 min) and SiO_2 (CF_4/O_2 = 33/1 sccm, 50 mTorr, 50 W, 3.5 min) layers.

2.3. Fabrication of the membrane-type transistor array

The process begins with preparing the printable substrate, which is discussed in the previous section. Then, a 65/5-nm-thick Au/Cr layer as a gate electrode is formed by DC sputtering (Ar = 15 sccm, 10 mTorr, 330/260 V), photolithography, and wet etching. A 100-nm-thick SiO_2 dielectric layer is formed by PECVD, followed by photolithography and a dry etching process using a reactive ion etching system (RIE, VACUUM SCIENCE) for SiO_2 (same conditions as above). Next, a 15-nm-thick IGZO channel is formed by RF sputtering (Ar/O_2 = 15/0.15 sccm, 2.5 mTorr, 50 W), an annealing process in a furnace (air, 0.3 L/min, 300 °C, 100 min), photolithography and wet etching (vol. ratio HCl:DI water = 50:1). Then, as the source and drain electrodes, 10-nm-thick Cr and 90-nm-thick Au layers are formed using DC sputtering, followed by a lift-off process. Moreover, spin coating (3000 rpm, 15 s) of a diluted SU-8 precursor solution (vol. ratio for SU-8 2010:SU-8 thinner = 9:1, MICRO CHEM) with prebaking (95 °C, 5 min), UV exposure, postexposure baking (95 °C, 15 min), development (SU-8 developer, MICRO CHEM), and hard baking (200 °C, 5 min) processes forms a 100-nm-thick SU-8 passivation layer. After additional 1.4-μm-thick PI and 100-nm-thick SiO_2 layers are formed using the aforementioned method to encapsulate the IGZO transistor array, the aforementioned dry etching process opens the contact pads.

2.4. Lamination of electronic devices to frameworks

The bottom Ecoflex surface of the plastic-elastomer framework is activated with O_2 plasma via RIE (O_2 = 20 sccm, 100 mTorr, 50 W, 5 sec), cast with 2 vol% (3-glycidyloxypropyl)trimethoxysilane (GPTMS) (Sigma Aldrich) in DI water, rinsed with DI water, and blow-dried. The top SiO_2 surface of the fabricated electronics is activated with O_2 plasma treatment, then cast with 2 vol% (3-aminopropyl)trimethoxysilane (APTMS) (Sigma Aldrich) in DI water for 20 min, finally rinsed with DI water and blow-dried. Then, the amino/epoxy-anchored surfaces are placed facing each other and gently put in contact to attain conformal contact for the bonding process (at room temperature, for 1 h). After the edges of the bonded specimen are trimmed off with a razor, the specimen is immersed in a warm DI water bath (55 °C for over 12 h) to eliminate the GeO_x layer and gently retrieved with tweezers, followed by a drying process under ambient conditions.

2.5. Mechanical and electrical characterization

The peel strength-distance curve is obtained using a universal test machine (UTM, TO-100-IC, TESTONE, pulling speed: 10 mm/min, load: 10 kgf). The I-V curves of the electrode are obtained by using a semiconductor parameter analyzer (Agilent B1500A, Agilent Technologies, Santa Clara, CA, USA). The representative transfer (I_{DS}-V_{GS}) curves of the IGZO-based transistor array are obtained with a semiconductor parameter analyzer (Agilent B1500A, Agilent Technologies, Santa Clara, CA, USA).

2.6. Numerical simulations

Mechanical FEM simulation is performed by COMSOL Multiphysics 6.0. The material parameters used for SiO_2, IGZO, SU-8, ABS, PI, and Au are based on the values in the literature and the material library in COMSOL [33]. The hyperelastic material parameters for Ecoflex are obtained by fitting an experimental tensile stress–strain curve (Fig. S1 in the Supplementary materials) to the Ogden model [42]. Tetrahedral meshes are used for 3D simulation of ABS-Ecoflex frameworks, and mapped meshes are used for cross-sectional 2D simulation of ABS-Ecoflex-electrode and ABS-Ecoflex-IGZO transistors. A static solver is used for all simulations with prestress values stepwise increased by 0.01 MPa.

3. Results and discussion

3.1. Development of 3D electronics based on plastic-elastomer frameworks

Fig. 1 illustrates the fabrication procedure to develop 3D electronics (IGZO transistor array as a representative). Briefly, the process begins with ESP of ABS on a glass substrate using a 3D printer to generate an ABS line array with residual shear stress (Fig. 1a); the thickness (T_{ABS}) and width (W_{ABS}) of the stressed ABS lines are fixed at 150 μm and 850 μm, respectively, for the rest of this study, while the length of ABS (L_{ABS}) is desirably controlled. The stressed ABS lines are treated with atmospheric surface plasma and ATMS in sequence to obtain an allyl-anchored ABS surface (Fig. 1b) [43,44]. Then, by drop-casting a silicone rubber crosslinker (Sylgard184 B) on the allyl-anchored ABS, a Sylgard184 B-anchored surface can be achieved (Fig. 1c). The surface-modified ABS lines are placed on a PET film and coated with an Ecoflex precursor mixture to finalize the plastic-elastomer framework fabrication (Fig. 1d). After peeling off the framework from the PET film (Fig. 1e), O_2 plasma surface and GPTMS treatment of the backside of the framework generate an epoxy-terminated surface for lamination with a device layer (Fig. 1f). Separately, after a printable device layer with a membrane-type IGZO transistor array is developed on a handling silicon wafer with a sacrificial GeO_x layer using the method explained in the Experimental methods, the top surface is covered with an SiO_2 layer to allow the lamination process with the plastic-elastomer framework (Fig. 1g). Then, the SiO_2 top surface of the device layer is treated with O_2 plasma and ATPMS to generate an amine-terminated surface (Fig. 1h). Conformal contact between the device layer and plastic-elastomer framework allows lamination with solid amine-epoxy interfacial bonds (Fig. 1i) [44]. After removal of the sacrificial layer (GeO_x), the sample is retrieved (Fig. 1j) and annealed at 120 °C for 1 h to transform it into a 3D structure through relaxation of shear-printed ABS (Fig. 1k).

3.2. Interface enhancement of plastic-elastomer frameworks

Before investigating the control parameters of plastic-elastomer frameworks to obtain desirable curvatures, guaranteeing reliable interfacial adhesion between the ABS and the Ecoflex and preventing unwanted interfacial delamination arising from the stress accumulated during the annealing and deformation process are crucial. The core technology for solid interfacial adhesion in this study is to use the SAM of ATMS formed on the surface of ABS and further modify the surface with Sylgard184 B to provide sufficient crosslinking sites for other silicone rubber coatings, such as Ecoflex. Fig. 2a shows the X-ray photoelectron spectroscopy (XPS)

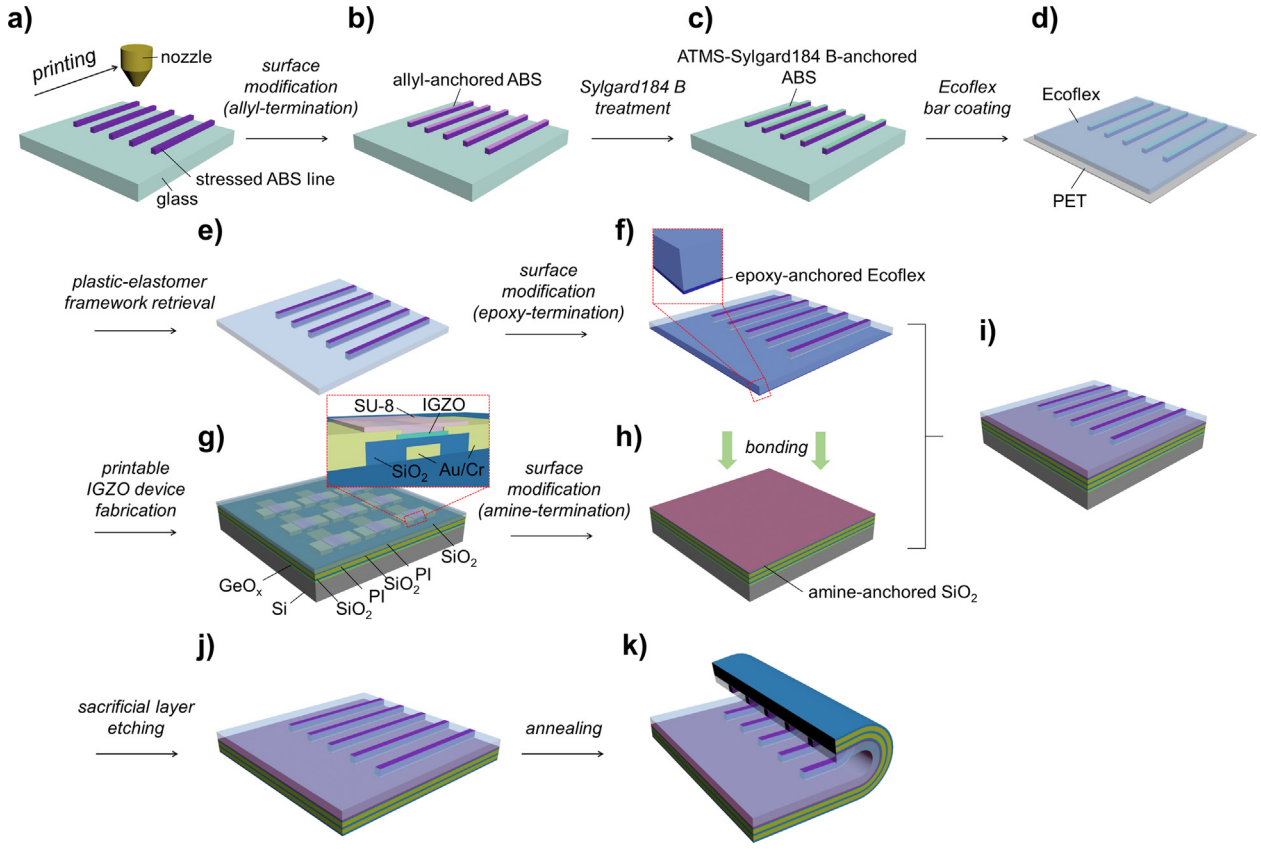

Fig. 1. Schematic diagram of developing a 3D IGZO transistor array. a) to e) Fabrication processes to develop a plastic-elastomer framework. f) to i) Surface modification and bonding process between a membrane-type IGZO transistor array and the plastic-elastomer framework using an SAM. j) and k) Shape-morphing process with thermal relaxation of stressed ABS lines in the plastic-elastomer framework.

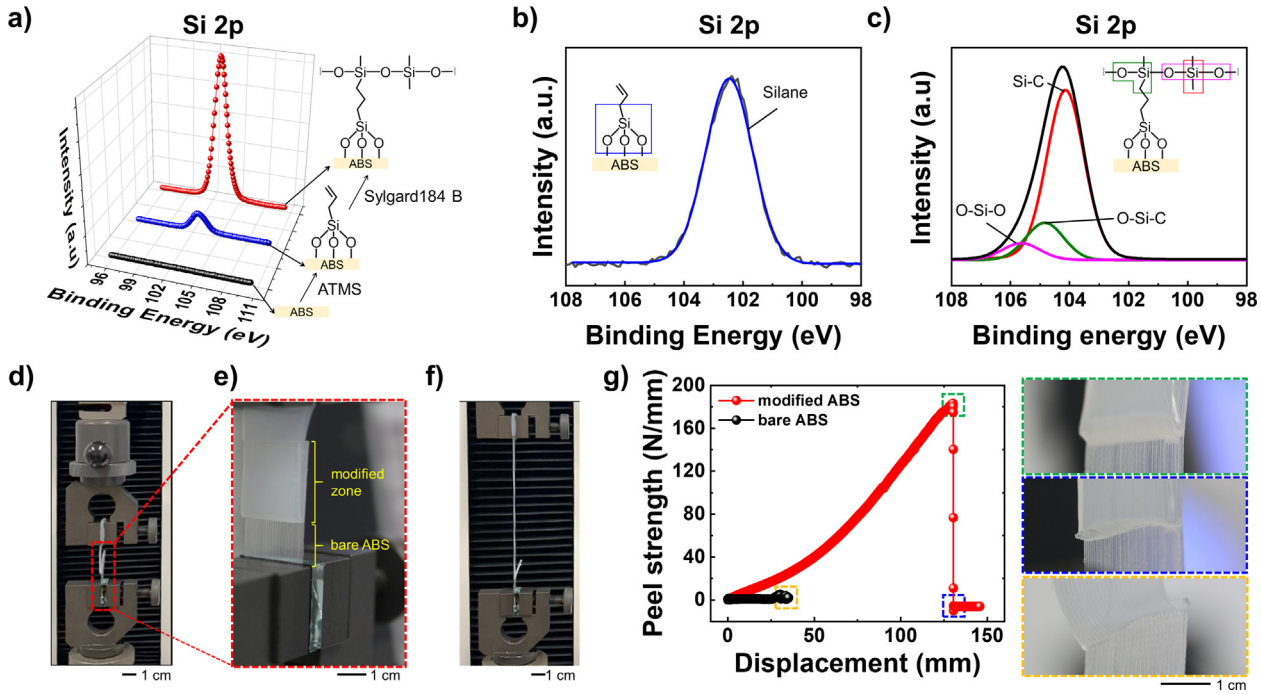

Fig. 2. XPS analyses of Si 2p peaks for the a) bare (black), ATMS-modified (blue), and ATMS-Sylgard184 B-modified (red) ABS surfaces. Core-level Si 2p spectra of b) ATMS-modified and c) ATMS-Sylgard184 B-modified ABS surfaces. Photographs of d) the initial setup with a specimen with an ATMS-Sylgard184 B-modified ABS surface, e) magnified image of the specimen (red box in Fig. 2d), and f) the specimen close to the breakpoint. g) Peel strength-displacement curves and photographs of the specimens at different stages of the peel test denoted by the colored dashed boxes. (For interpretation of the references to colour in this figure legend, the reader is referred to the web version of this article.)

spectra of Si 2p for tracing the stepwise formation of the SAM and silicone rubber crosslinker on the surface of ABS. At first glance, the bare ABS (black line) surface has no observable peak corresponding to Si 2p, whereas the ATMS-modified (blue line) and ATMS-Sylgard184 B-modified (red line) surfaces exhibit significant Si 2p peaks. Fitting of the Si 2p core-level spectrum for the ATMS-modified surface in Fig. 2b shows that the sharp feature at a binding energy of 102.38 eV corresponds to silanes (SiO_3C) [45], confirming ATMS formation because the first atmospheric surface plasma treatment of the ABS surface enriches hydroxyl groups to allow a coupling reaction with ATMS to form Si-O-C linkages [46]. In contrast, the fitting of the Si 2p core-level spectrum of the ATMS-Sylgard184 B-treated surface shows three main peaks at 104.15 eV, 104.84 eV, and 105.61 eV, corresponding to Si-C, O-Si-C, and O-Si-O linkages, respectively, confirming the formation of the ATMS-Sylgard184 B-modified surface (Fig. 2c). Furthermore, the Fourier transform infrared (FTIR) spectra clearly show the existence of Si-CH_3 [47] at 1261 cm^{-1} for the case of the ATMS-Sylgard184 B-modified surface, whereas the ATMS-anchored surface shows no signs of such a peak, which proves the successful anchoring of the silicone crosslinker; see Fig. S2 (Supplementary materials).

A mechanical peel test is also carried out on the ABS-Ecoflex bilayer films (W_{ABS}: 2 cm, L_{ABS}: 4 cm, T_{ABS}: 500 μm) with or without surface treatment; see the representative setup in Fig. 2d. Briefly, the specimens are prepared under two conditions: use of a bare ABS film for the Ecoflex curing process and use of ATMS-Sylgard184 B modification for the Ecoflex curing process. In the latter case, the ABS surface is partially modified to form a fine boundary to determine any interfacial delamination above the boundary (see the photographic images in Fig. 2e and 2f). Without surface modification, only a peel strength of 5.30 N/mm is required to gently detach the Ecoflex film from the bare ABS (Fig. 2g). In contrast, with surface modification, only part of the Ecoflex film up to the boundary is elongated up to 183 N/mm, with no significant interfacial delamination in the region above the boundary until the breakpoint (Fig. 2g); see the photographic images of the specimens at different stages of the peel test denoted by the colored dashed boxes (green: maximum elongation of Ecoflex in the modified ABS specimen, blue: cohesive fracture of Ecoflex in the modified ABS specimen, yellow: delamination of Ecoflex in the bare ABS specimen). This result confirms the reliable, solid interfacial adhesion for further study of the mechanical deformation of plastic-elastomer frameworks in a stable manner. We note that all the samples hereafter are prepared with the surface treatment for solid interfacial adhesion.

3.3. Control parameters for shape morphing

Next, determining the stable annealing temperature (T_{anneal}) and annealing time (t_{anneal}) to achieve the desired shape of a framework is also important because such an annealing process induces not only thermal relaxation of the printed stressed ABS lines but also thermal expansion of the Ecoflex itself, which disturbs the shape change. Fig. 3a presents the geometric structure of the plastic-elastomer framework. As a test sample, a simple framework with a simple stressed ABS line embedded in one side of an Ecoflex film structure [length of Ecoflex ($L_{Ecoflex}$) = 19 mm, width of Ecoflex ($W_{Ecoflex}$) = 6 mm, thickness of Ecoflex ($T_{Ecoflex}$) = 900 μm, length of ABS (L_{ABS}) = 19 mm, width of ABS (W_{ABS}) = 850 μm, thickness of ABS (T_{ABS}) = 150 μm] is prepared, as shown in Fig. 3b. When the framework is annealed around or above the T_g (113 °C) [33] of ABS, the stressed polymer chains naturally contract to force bending of the overall structure of the framework without peeling or gap formation at the plastic-elastomer interface; see a representative sample with an inner curvature (k_{inner}) of 0.24 mm^{-1} under the conditions of T_{anneal} = 120 °C and t_{anneal} = 60 min (Fig. 3c). Fig. 3d and Fig. S3 (Supplementary materials) show the k_{inner} of the framework as a function of T_{anneal} (e.g., 100 °C, 120 °C, 140 °C, and 160 °C) and t_{anneal} (from 0 to 180 min). At 100 °C, the framework starts to slightly bend, having a k_{inner} of 0.0088 mm^{-1} at 4 min, and slightly further bends for a prolonged t_{anneal} (k_{inner} = 0.012 mm^{-1} at 180 min). This observation indicates that the temperature around T_g induces slow contraction of the stressed ABS lines during the annealing process. At 120 °C, k_{inner} becomes 0.027 mm^{-1} at t_{anneal} = 1 min, increases to 0.20 mm^{-1} at 60 min, is maintained for 1 h further, and slowly decreases to 0.19 mm^{-1} at 180 min. For higher temperatures (e.g., 140 °C and 160 °C), k_{inner} rapidly increases up to 0.19 and 0.18 mm^{-1}, respectively, for the first few minutes of t_{anneal} (4 min and 2 min for 140 °C and 160 °C) and then decreases back to flat (k_{inner} = 0 mm^{-1}). Such a high annealing temperature range does not guarantee mechanical stability after bending due to the significant thermal expansion of the Ecoflex, which forces the bent framework into a planar structure. As a result, we confirm that the optimum T_{anneal} and t_{anneal} are 120 °C and 60 min. In our system, when the shape morphed plastic-elastomer framework is cooled below T_g, the contracted polymer chains change state from the viscoplastic state to the glassy state, maintaining the deformed shape. The plastic-elastomer framework exposed to 120 °C for 60 min is cooled to room temperature. To confirm the shape fixity ratio, each curvature of the framework before and after cooling is compared, and the calculated shape fixity ratio is 94% (k_r/ k_h × 100%, where k_r and k_h are the maximum curvatures of the specimen at room temperature and 120 °C, respectively). The slight shape change of 6% seems to be caused by the difference in thermal expansion coefficients of ABS and Ecoflex (Fig. S4, Supplementary materials). The thickness ratio also influences the degree of bending after the annealing process because comparably thick Ecoflex resists the bending force. Annealing and bending five frameworks with Ecoflex of various thicknesses ($L_{Ecoflex}$ = 20 mm, $W_{Ecoflex}$ = 600 μm, $T_{Ecoflex}$ = 520, 820, 1200, 2100, and 3100 μm) and with stressed ABS lines (L_{ABS} = 19 mm, fixed) result in k_{inner} values of 0.46, 0.20, 0.14, 0.025 and 0.0085 mm^{-1}, respectively (Fig. 3e); we note that these values are the highest values obtained up to a t_{anneal} of 60 min.

We can also control the degree of bending curvature through the ABS printing speed (V_{ESP}) because a higher shear rate induces higher residual stress of ABS, resulting in higher curvatures. For demonstration, all the samples are set to have an ABS stressed line prepared at various shear rates (100, 200, 600, 1000, 2000, and 3000 s^{-1}) embedded in one side of the Ecoflex film with a fixed geometry ($L_{Ecoflex}$ = 19 mm, $W_{Ecoflex}$ = 6 mm, $T_{Ecoflex}$ = 820 μm); the V_{ESP} values corresponding to shear rates of 100, 200, 600, 1000, 2000, and 3000 s^{-1} are 5, 10, 30, 50, 100, and 150 mm/s. Annealing the samples (T_{anneal} = 120 °C and t_{anneal} = 60 min) results in k_{inner} = 0.12, 0.12, 0.13, 0.17, and 0.28 mm^{-1}, respectively (Fig. 4a and 4b).

To develop desirable 3D electronics based on the ABS-Ecoflex framework, a large Ecoflex film must be used to mount membrane-type electronic devices, and multiple stressed ABS lines must be embedded inside the film to control the curvature of the framework after bending. In this case, the pitch of the stressed ABS lines becomes a control parameter. As a simple example, we designed an ABS-Ecoflex framework with parallelly aligned ABS stressed lines, expecting a final cylindrical structure after the annealing process (T_{anneal} = 120 ℃ and t_{anneal} = 60 min). Naturally, the pitch of stressed ABS lines should play a crucial role in controlling the curvature of the cylinder. Fig. 4c describes the curvature of the cylindrical structure as a function of the line pitch; the maximum curvature (k_{max}, the curvature where the stressed ABS lines are printed) and minimum curvature (k_{min}, the curvature in the

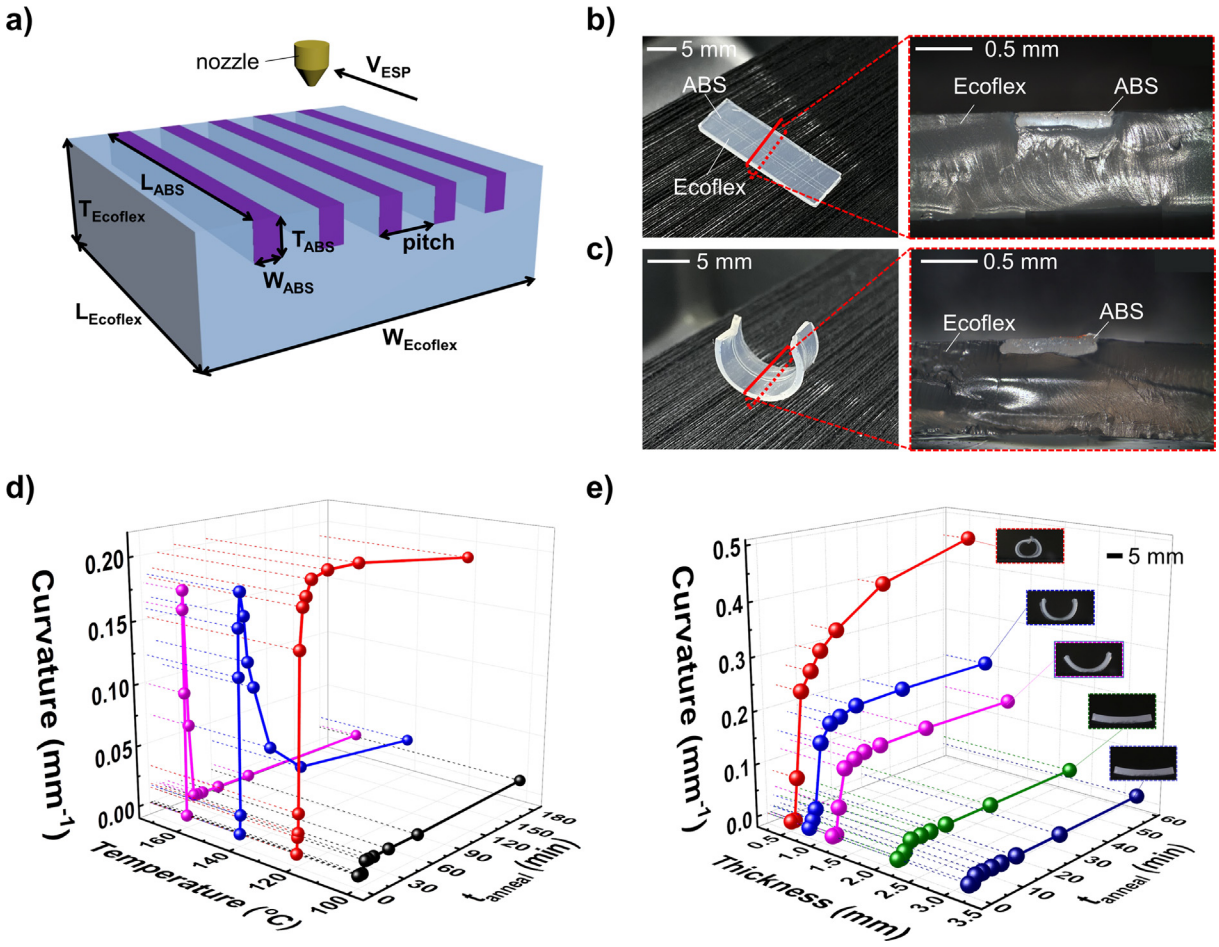

Fig. 3. a) schematic diagram of an ABS-ecoflex framework with parameters. photographs of an ABS-ecoflex framework b) before and c) after transformation. the selected red boxes are corresponding cross-sectional microscopic images of the framework. d, e) curvatures (k) of plastic-elastomer frameworks as a function of d) the annealing time (t_{anneal}) at various temperatures and e) t_{anneal} at different Ecoflex thicknesses. (For interpretation of the references to colour in this figure legend, the reader is referred to the web version of this article.)

middle between the stressed ABS lines) are measured. k_{min} increases as the pitch of the stressed ABS lines decreases; as the pitch decreases from 12 mm to 2 mm, k_{min} increases from 0.094 to 0.44 mm^{-1}. The relative difference between k_{max} and k_{min} increases from 8.7% to 44% as the pitch of the stressed ABS lines changes from 2 mm to 12 mm, which means that more significant curvature fluctuation occurs at larger pitches of ABS stressed lines, as shown in Fig. 4d. Based on the simple bending behavior of the plastic-elastomer framework, we can develop various 3D structures.

3.4. 3D shape morphing with various Gaussian curvatures

Shape morphing into 3D structures with various Gaussian curvatures is possible using geometrically designed stressed ABS lines. For example, placing stressed ABS line arrays on the top and left-hand side and on the bottom and right-hand side of Ecoflex allows reverse bending about the desired axes (Fig. 5a). Moreover, other planar frameworks, such as a spiral stressed ABS line on the top surface of circular Ecoflex (Fig. 5b), two stripe stressed ABS line arrays in orthogonal directions on the top and bottom surfaces of square Ecoflex (Fig. 5c), and a mesh pattern with a circular outline of stressed ABS lines on circular Ecoflex (Fig. 5d), can change to complex 3D structures, such as bent, cone, saddle, and dome shapes, respectively. Mechanical finite element method (FEM) simulation is useful to comprehend the shape morphing behavior during the thermal annealing process. Static FEM analysis consisting of an elastoplastic model for ABS and a hyperelastic model for Ecoflex is performed with the material properties. At 50 ℃, i.e., the curing temperature of Ecoflex, which we set in the initial stage of the simulation, stressed ABS lines (range of stress values of the ABS lines: 0.05 to 0.4 MPa) have no deformation due to their high elastic modulus (~2.2 GPa), and the cured Ecoflex has zero stress. Then, the annealing process at 120 ℃ reduces the elastic modulus of ABS to ~ 2.9 MPa and induces large strains in the ABS lines (strain range of the ABS lines changed from the initial shape: −20.5% to 16.9%) due to the thermal relaxation of the stressed ABS lines. During shape deformation, stress equilibrium decreases the stress level of ABS lines from the initial values and increases the stress level of Ecoflex from zero (see separate stress distribution maps of ABS and Ecoflex in Fig. S5, Supplementary materials). Moreover, thermal expansion generates additional stresses (increase rate of the maximum von Mises stress: 0.4 to 15.1%; see Table T1 and Fig. S6 in the Supplementary materials) through the difference in the coefficient of thermal expansion (CTE) of ABS (76 ppm/℃) [48] and Ecoflex (284.2 ppm/℃) [49].

3.5. Electronics-level 3D shape morphing

In the next step, the transformation of ABS-Ecoflex frameworks should guarantee stability at the electronic device level. As a first test sample, a membrane-type Au/Cr electrode [90 nm

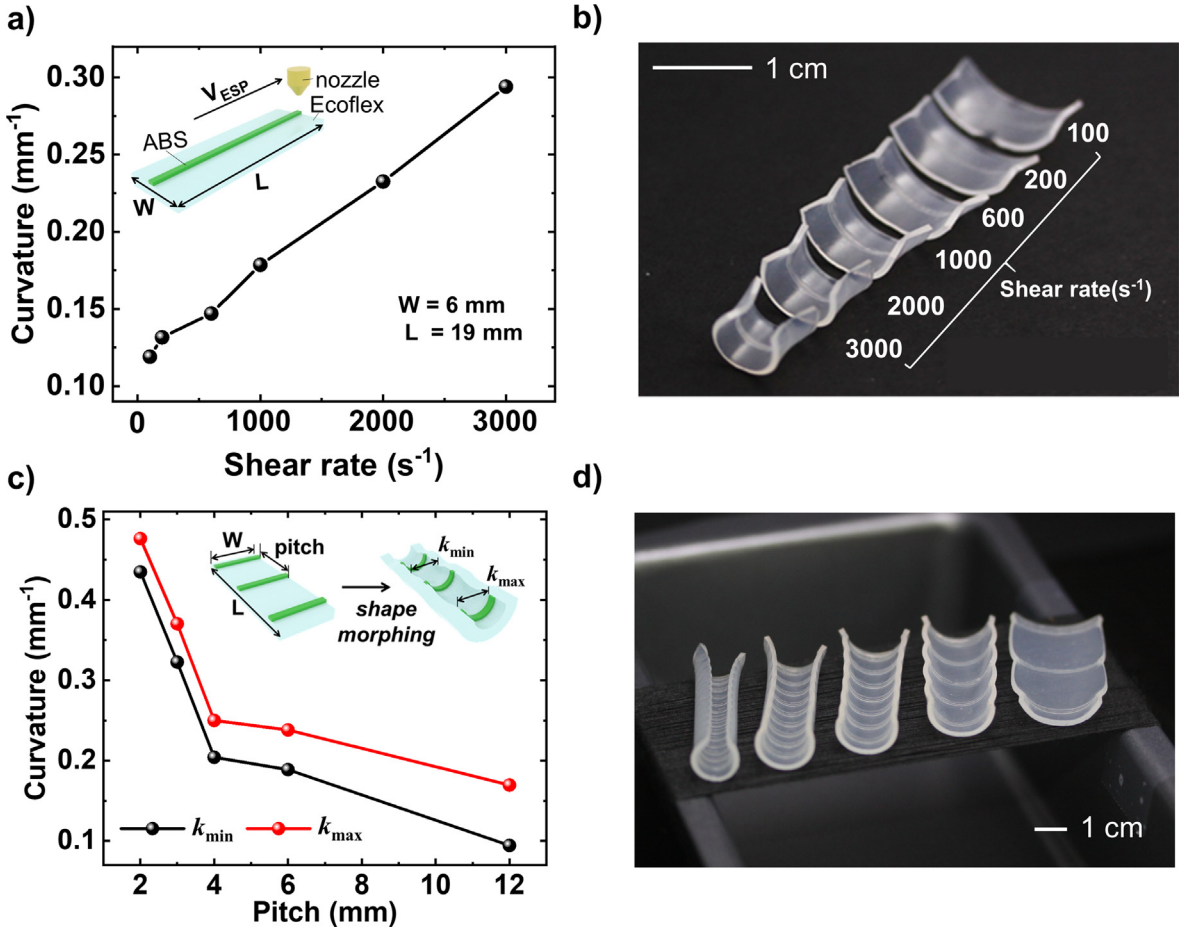

Fig. 4. a) Curvatures (k) of ABS-Ecoflex frameworks as a function of the shear rate, and b) corresponding photograph after thermal relaxation. c) Curvatures (k) of ABS-Ecoflex frameworks as a function of the line printing pitch, and d) photograph of the representative shape-morphed frameworks after deformation.

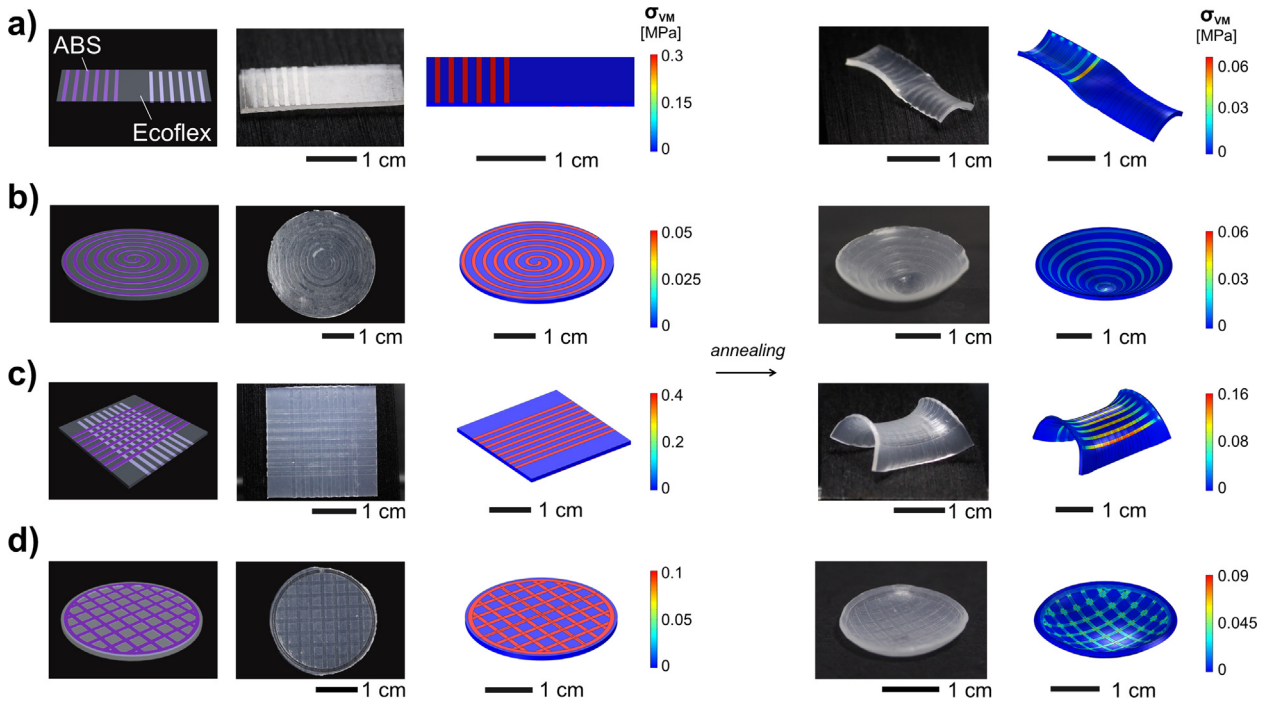

Fig. 5. Schematic illustrations, photographs, and von Mises stress distribution maps obtained by FEM simulation of ABS-Ecoflex frameworks with various geometrical designs (left) before and (right) after thermal relaxation. Stressed ABS line designs allow shape morphing of the ABS-Ecoflex frameworks to a) a reverse bend, b) a cone, c) a saddle, and d) a dome. FEM simulation data are obtained at 50 °C (left) and 120 °C (right).

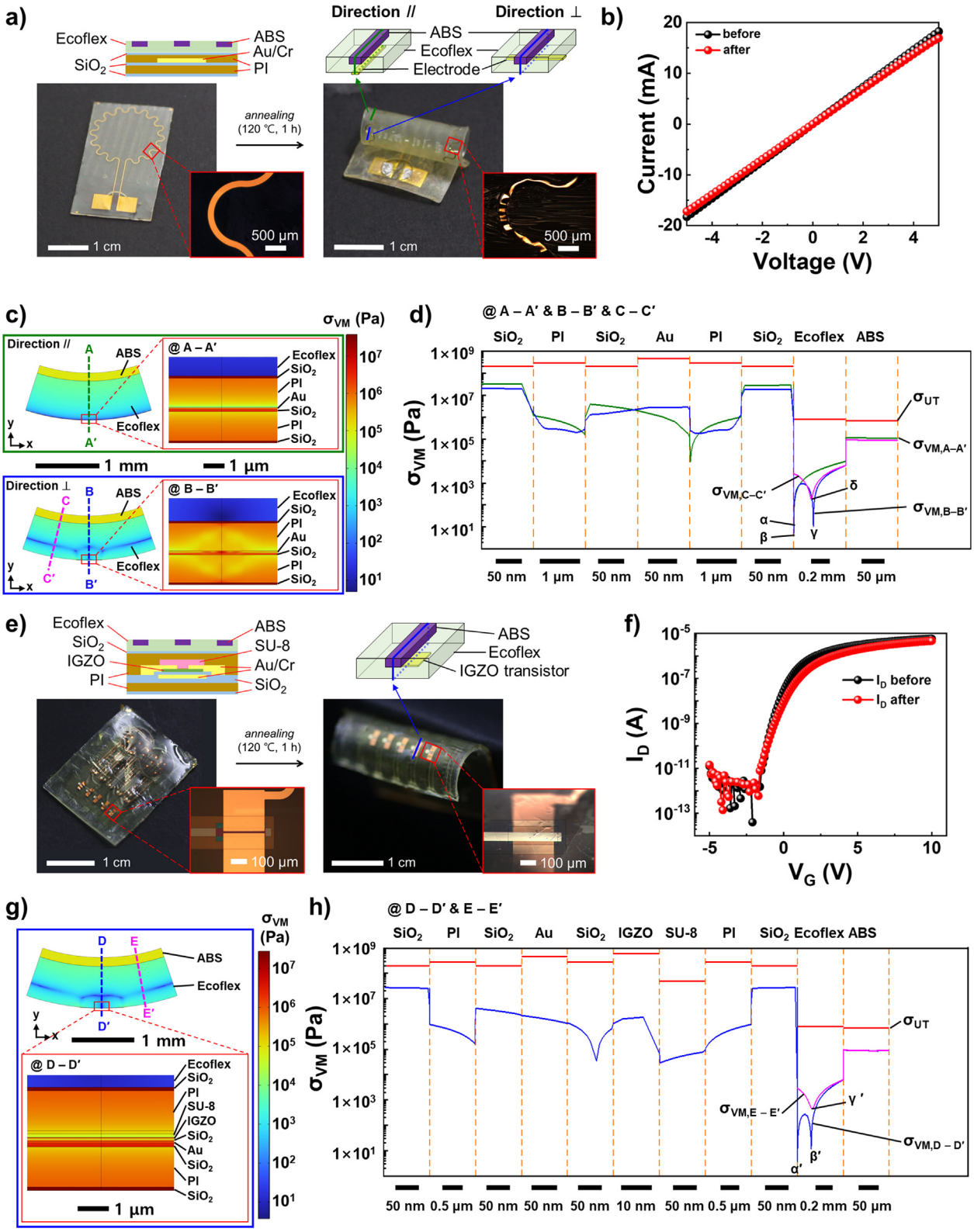

Fig. 6. Electrical performance and mechanical FEM simulation results of a Au/Cr electrode and IGZO transistors before and after shape morphing. a) and b) Photograph/optical microscopy images and I-V characteristics of the Au/Cr electrode mounted on the ABS-Ecoflex framework. c) and d) von Mises stress distribution maps and vertical σ_{VM} profiles (denoted by A-A′, B-B′, and C-C′ in Fig. 6c) of the ABS-Ecoflex framework with the Au/Cr electrode after shape morphing; green and blue colored boxes correspond to the parallel and perpendicular directions. e) and f) Photograph/optical microscopy images and representative I_D–V_G transfer curves at V_D = 1 V of IGZO transistors mounted on the ABS-Ecoflex framework. g) and h) von Mises stress distribution maps and vertical σ_{VM} profiles (denoted by D-D′ and E-E′ in Fig. 6g) of the ABS-Ecoflex framework with an IGZO transistor after shape morphing. Cross-sectional illustrations of the specimens are added in Fig. 6a and 6e. The ultimate stress (σ_{UT}, red lines) of each material and the minimal stress points (denoted by the symbols α, β, γ and δ) at the interface and inside Ecoflex are added in Fig. 6d and 6 h. The Cr layer is ignored in the FEM simulation for simplicity. (For interpretation of the references to colour in this figure legend, the reader is referred to the web version of this article.)

(top)/10 nm (bottom), Cr layer used as an adhesive layer] with a global circular shape and a local serpentine pattern is mounted onto an ABS-Ecoflex framework, and the resistance is measured before and after 3D shape morphing; the more detailed fabrication process is described in the Experimental methods and Fig. S7 (Supplementary materials). Briefly, the ABS lines are prepared by ESP at a shear rate of 1000 s^{-1} and a line pitch of 2 mm to develop the ABS-Ecoflex framework; we note that simple straight ABS line arrays are used to demonstrate morphing of the electrode into a cylindrical shape with a maximum curvature = 0.39 mm^{-1}, which is the most extreme stress condition including morphing to the various Gaussian curvature shapes demonstrated in Fig. 5 (Fig. S8, Supplementary materials). The ABS-Ecoflex framework is treated with GPTMS. Separately, membrane-type electronic devices are prepared on a polyimide (PI) substrate and encapsulated by an additional PI layer. After a SiO_2 layer is deposited on the top PI layer, the device layer is treated with APTMS. After lamination of the two layers at room temperature, the sample is annealed at 120 °C to induce shape morphing (Fig. 6a); we note that the planar region for the sample corresponds to the ABS line-free region for easy access to probe the contact pads. The metal line is still conductive with only a slight increase in the resistance (5.82%) from 273 mΩ to 289 mΩ after bending (Fig. 6b). According to the optical microscopy image, a wrinkled structure appears, but there are no cracks in the metal electrode after bending (Fig. S9, Supplementary materials).

A cross-sectional FEM simulation of the electrode-ABS-Ecoflex specimen is carried out to confirm the mechanical stability during shape morphing. Two different cross-sections in the specimen are selected, as shown in Fig. 6a; see the green and blue lines with the symbols // and ⊥ meaning parallel and perpendicular directions of the electrode lines with respect to an ABS line. In the selected cross-sections, the parallelly aligned electrode line covers the whole bottom, while the perpendicularly aligned electrode line partially covers the bottom (Fig. 6c). All the von Mises stresses ($\sigma_{VM,//,A\text{-}A'}$, $\sigma_{VM,\perp,B\text{-}B'}$, and $\sigma_{VM,\perp,C\text{-}C'}$) in the regions denoted by A-A′, B-B′and C-C′ are lower than the ultimate stresses (σ_{UT}) of the related materials (Fig. 6d). As expected, the soft Ecoflex adjusts the stress distribution depending on the existence and even positions of the electrode layer. With the parallel electrode line, the Ecoflex corresponding to A-A′ has the minimum stress ($\sigma_{VM,//,A\text{-}A',\alpha\text{-}min}$ = 13.1 Pa) at the SiO_2/Ecoflex interface (denoted by α) owing to suppression of the deformation of Ecoflex by perfect binding to rigid materials. With the perpendicular electrode layer, the points of minimal von Mises stress are located differently depending on the position. In the region immediately above the perpendicular electrode line (corresponding to B-B′), Ecoflex has double minimum peaks; one ($\sigma_{VM,\perp,B\text{-}B',\beta\text{-}min}$ = 4.87 Pa) appears at the SiO_2/Ecoflex interface (denoted by β) due to the rigidity of the device layer, and the other ($\sigma_{VM,\perp,B\text{-}B',\gamma\text{-}min}$ = 10.8 Pa) lies inside the Ecoflex (denoted by γ) due to balancing of the local stress components of the Ecoflex layer. In the region above the electrode-free area (C-C′), Ecoflex has the minimum value of σ_{VM} ($\sigma_{VM,\perp,C\text{-}C',\delta\text{-}min}$ = 179 Pa) at a level below the middle of the Ecoflex (denoted by δ).

As a second test sample, we developed a printable layer with an IGZO-based transistor array; see the more detailed fabrication process in the Experimental methods and Fig. S10 (Supplementary materials). After the surface modification and lamination processes of the device layer and ABS-Ecoflex framework described for the Au/Cr electrode, the sample is transformed into a cylindrical shape (curvature of 0.38 mm^{-1}) at 120 °C (Fig. 6e). We note that five transistors are produced in the fabrication processes; four transistors are used to check if each fabrication and transfer printing process is properly performed. The other is used to measure the electrical properties before and after deformation. As shown in Fig. 6f, there is no significant degradation in the transfer characteristics (I_D–V_G) at V_D = 1 V after the shape deformation. The current on/off ratios (I_{on}/I_{off}), threshold voltages (V_{th}), and field-effect mobilities (μ_{FE}) extracted from the I_D-V_G curves before and after shape deformation are 1.26 × 10^7 and 8.69 × 10^6, 0.57 V and 1.49 V, and 0.79 $cm^2\ V^{-1}\ s^{-1}$ and 0.63 $cm^2\ V^{-1}\ s^{-1}$, respectively.

Mechanical stress analysis by FEM simulation is carried out to obtain insight into the mechanical stability of the IGZO transistor after shape morphing (Fig. 6g). In the cross-section (denoted by D-D′) at the center of the device layer, two minimal von Mises stress values are located at the SiO_2/Ecoflex interface ($\sigma_{VM,D\text{-}D',\alpha'\text{-}min}$ = 3.74 Pa) and inside the Ecoflex ($\sigma_{VM,D\text{-}D',\beta'\text{-}min}$ = 11.6 Pa), while the cross-section away from the device layer (denoted by E-E′) has one minimal stress value ($\sigma_{VM,E\text{-}E',\gamma'\text{-}min}$ = 448 Pa) inside the Ecoflex (Fig. 6h). This result indicates that the soft elastomer adjusts the stress distribution to reduce the mechanical stress of the components in the IGZO transistor to levels much below their σ_{UT}s during shape morphing.

4. Conclusions

In summary, combining shear-printed ABS lines and Ecoflex offers versatile frameworks that can implement planar electronic devices and shape morphing into complex 3D architectures with various Gaussian curvatures. Systematic surface modification of ABS and Ecoflex with reactive silanes strengthens the interfacial adhesion, which is robust to shape morphing through a thermal relaxation process and even a harsh peel test. The annealing temperature, relative thickness ratio between ABS and Ecoflex, shear rate of ESP, and pitch of ABS lines offer control parameters to develop desired complex 3D structures. Furthermore, the combination of ABS lines with an array, spiral, biaxial, or mesh configuration allows transformation into various Gaussian curvatures, such as a bend, a cone, a saddle, and a dome. The successful demonstration of mounting a membrane-type Au/Cr electrode and an IGZO transistor array onto ABS-Ecoflex frameworks and further transformation without electrical failure shows the feasibility of this method for 3D electronics.

Data availability

Data will be made available on request.

CRediT authorship contribution statement

Jung Il Yoo: Conceptualization, Data curation, Formal analysis, Investigation, Writing – original draft. **Dukkyu Park:** Data curation, Formal analysis, Investigation, Methodology, Writing – original draft, Writing – review & editing. **Seung Hyun Kim:** Formal analysis, Investigation. **Seonggwang Yoo:** Formal analysis, Investigation. **Hun Soo Jang:** Project administration, Formal analysis, Writing – original draft. **Jongwon Yoon:** Project administration, Data curation, Writing – original draft. **Heung Cho Ko:** Conceptualization, Funding acquisition, Project administration, Supervision, Writing – original draft, Writing – review & editing.

Declaration of Competing Interest

The authors declare that they have no known competing financial interests or personal relationships that could have appeared to influence the work reported in this paper.

Acknowledgments

This work was supported by a National Research Foundation of Korea (NRF) grant funded by the Korean government (MSIT) (No.

2021R1A2C2093380), the GIST Research Project grant funded by the GIST in 2022, and the Fundamental Research Program (PNK9020) of the Korea Institute of Materials Science (KIMS).

Appendix A. Supplementary data

Supplementary data to this article can be found online at https://doi.org/10.1016/j.matdes.2023.111811.

References

[1] H.C. Ko, M.P. Stoykovich, J. Song, V. Malyarchuk, W.M. Choi, C.-J. Yu, J.B. Geddes III, J. Xiao, S. Wang, Y. Huang, J.A. Rogers, A hemispherical electronic eye camera based on compressible silicon optoelectronics, Nature 454 (2008) 748–753.

[2] H.S. Jang, G.-G. Kim, S.H. Kang, Y. Kim, J.I. Yoo, S. Yoo, K.-K. Kim, C. Jung, H.C. Ko, A Bezel-Less Tetrahedral Image Sensor Formed by Solvent-Assisted Plasticization and Transformation of an Acrylonitrile Butadiene Styrene Framework, Adv. Mater. 30 (2018) 1801256.

[3] M.S. Kim, G.J. Lee, C. Choi, M.S. Kim, M. Lee, S. Liu, K.W. Cho, H.M. Kim, H. Cho, M.K. Choi, N. Lu, Y.M. Song, D.-H. Kim, An aquatic-vision-inspired camera based on a monocentric lens and a silicon nanorod photodiode array, Nat. Electron. 3 (2020) 546–553.

[4] C. Choi, J. Leem, M.S. Kim, A. Taqieddin, C. Cho, K.W. Cho, G.J. Lee, H. Seung, H.J. Bae, Y.M. Song, T. Hyeon, N.R. Aluru, S. Nam, D.-H. Kim, Curved neuromorphic image sensor array using a MoS_2-organic heterostructure inspired by the human visual recognition system, Nat. Commun. 11 (2020) 5934.

[5] Y.M. Song, Y. Xie, V. Malyarchuk, J. Xiao, I. Jung, K.-J. Choi, Z. Liu, H. Park, C. Lu, R.-H. Kim, R. Li, K.B. Crozier, Y. Huang, J.A. Rogers, Digital cameras with designs inspired by the arthropod eye, Nature 497 (2013) 95.

[6] L. Gu, S. Poddar, Y. Lin, Z. Long, D. Zhang, Q. Zhang, L. Shu, X. Qiu, M. Kam, A. Javey, Z. Fan, A biomimetic eye with a hemispherical perovskite nanowire array retina, Nature 581 (2020) 278–284.

[7] K. Zhang, Y.H. Jung, S. Mikael, J.-H. Seo, M. Kim, H. Mi, H. Zhou, Z. Xia, W. Zhou, S. Gong, Z. Ma, Origami silicon optoelectronics for hemispherical electronic eye systems, Nat. Commun. 8 (2017) 1782.

[8] G.-G. Kim, Y. Kim, S. Yoo, H.S. Jang, H.C. Ko, Hexahedral LED Arrays with Row and Column Control Lines Formed by Selective Liquid-Phase Plasticization and Nondisruptive Tucking-Based Origami, Adv. Mater. Technol. 5 (2020) 2000010.

[9] K. Sun, T.-S. Wei, B.Y. Ahn, J.Y. Seo, S.J. Dillon, J.A. Lewis, 3D Printing of Interdigitated Li-ion Microbattery Architectures, Adv. Mater. 25 (2013) 4539–4543.

[10] X. Liao, C. Shi, T. Wang, B. Qie, Y. Chen, P. Yang, Q. Cheng, H. Zhai, M. Chen, X. Wang, X. Chen, Y. Yang, High-Energy-Density Foldable Battery Enabled by Zigzag-Like Design, Adv. Energy Mater. 9 (2019) 1802998.

[11] M. Jo, S. Bae, I. Oh, J.-H. Jeong, B. Kang, S.J. Hwang, S.S. Lee, H.J. Son, B.-M. Moon, M.J. Ko, P. Lee, 3D Printer-Based Encapsulated Origami Electronics for Extreme System Stretchability and High Areal Coverage, ACS Nano 13 (2019) 12500–12510.

[12] Y. He, Z. Chen, S. Kong, Z. Mao, C. Yang, W. Wang, L. Wan, G. Liu, J. Yin, C.H. Chan, J. Lu, Light-controlled multifunctional reconfigurable structures, Appl. Mater. Today 26 (2022) 101393.

[13] J.J. Adams, E.B. Duoss, T.F. Malkowski, M.J. Motala, B.Y. Ahn, R.G. Nuzzo, J.T. Bernhard, J.A. Lewis, Conformal Printing of Electrically Small Antennas on Three-Dimensional Surfaces, Adv. Mater. 23 (2011) 1335–1340.

[14] B.L. Borgne, S. Liu, X. Morvan, S. Crand, R.A. Sporea, N. Lu, M. Harnois, Water Transfer Printing Enhanced by Water-Induced Pattern Expansion: Toward Large-Area 3D Electronics, Adv. Mater. Technol. 4 (2019) 1800600.

[15] D.-H. Kim, N. Lu, R. Ma, Y.-S. Kim, R.-H. Kim, S. Wang, J. Wu, S.M. Won, H. Tao, A. Islam, K.J. Yu, T.-I. Kim, R. Chowdhury, M. Ying, L. Xu, M. Li, H.-J. Chung, H. Keum, M. McCormick, P. Liu, Y.-W. Zhang, F.G. Omenetto, Y. Huang, T. Coleman, J.A. Rogers, Epidermal Electronics, Science 333 (2011) 838–843.

[16] D.-H. Kim, J. Viventi, J.J. Amsden, J. Xiao, L. Vigeland, Y.-S. Kim, J.A. Blanco, B. Panilaitis, E.S. Frechette, D. Contreras, D.L. Kaplan, F.G. Omenetto, Y. Huang, K.-C. Hwang, M.R. Zakin, B. Litt, J.A. Rogers, Dissolvable films of silk fibroin for ultrathin conformal bio-integrated electronics, Nat. Mater. 9 (2010) 511–517.

[17] D. Joung, K. Agarwal, H.-R. Park, C. Liu, S.-H. Oh, J.-H. Cho, Self-Assembled Multifunctional 3D Microdevices, Adv. Electron. Mater. 2 (2016) 1500459.

[18] W. Wang, C. Li, M. Cho, S.H. Ahn, Soft Tendril-Inspired Grippers: Shape Morphing of Programmable Polymer–Paper Bilayer Composites, ACS Appl. Mater. Interfaces 10 (2018) 10419–10427.

[19] S. Sundaram, D.S. Kim, M.A. Baldo, R.C. Hayward, W. Matusik, 3D-Printed Self-Folding Electronics, ACS Appl. Mater. Interfaces 9 (2017) 32290–32298.

[20] Q. Zhang, K. Zhang, G. Hu, Smart three-dimensional lightweight structure triggered from a thin composite sheet via 3D printing technique, Sci. Rep. 6 (2016) 22431.

[21] A.M. Abdullah, X. Li, P.V. Braun, J.A. Rogers, K.J. Hsiabdullah, Kirigami-Inspired Self-Assembly of 3D Structures, Adv. Funct. Mater. 30 (2020) 1909888.

[22] Y. Kim, H. Yuk, R. Zhao, S.A. Chester, X. Zhao, Printing ferromagnetic domains for untethered fast-transforming soft materials, Nature 558 (2018) 274–281.

[23] Q. Ze, X. Kuang, S. Wu, J. Wong, S.M. Montgomery, R. Zhang, J.M. Kovitz, F. Yang, H.J. Qi, R. Zhao, Magnetic Shape Memory Polymers with Integrated Multifunctional Shape Manipulation, Adv. Mater. 32 (2020) 1906657.

[24] Y. Liu, B. Shaw, M.D. Dickey, J. Genzer, Sequential self-folding of polymer sheets, Sci. Adv. 3 (2017).

[25] Y. Wang, M. Li, J.-K. Chang, D. Aurelio, W. Li, B.J. Kim, J.H. Kim, M. Liscidini, J.A. Rogers, F.G. Omenetto, Light-activated shape morphing and light-tracking materials using biopolymer-based programmable photonic nanostructures, Nat. Commun. 12 (2021) 1651.

[26] S. Xu, Z. Yan, K.-I. Jang, W. Huang, H. Fu, J. Kim, Z. Wei, M. Flavin, J. McCracken, R. Wang, A. Badea, Y. Liu, D. Xiao, G. Zhou, J. Lee, H.U. Chung, H. Cheng, W. Ren, A. Banks, X. Li, U. Paik, R.G. Nuzzo, Y. Huang, Y. Zhang, J.A. Rogers, Assembly of micro/nanomaterials into complex, three-dimensional architectures by compressive buckling, Science 347 (2015) 154–159.

[27] Z. Fan, Y. Yang, F. Zhang, Z. Xu, H. Zhao, T. Wang, H. Song, Y. Huang, J.A. Rogers, Y. Zhang, Inverse Design Strategies for 3D Surfaces Formed by Mechanically Guided Assembly, Adv. Mater. 32 (2020) 1908424.

[28] X. Wang, X. Guo, J. Ye, N. Zheng, P. Kohli, D. Choi, Y. Zhang, Z. Xie, Q. Zhang, H. Luan, K. Nan, B.H. Kim, Y. Xu, X. Shan, W. Bai, R. Sun, Z. Wang, H. Jang, F. Zhang, Y. Ma, Z. Xu, X. Feng, T. Xie, Y. Huang, Y. Zhang, J.A. Rogers, Freestanding 3D Mesostructures, Functional Devices, and Shape-Programmable Systems Based on Mechanically Induced Assembly with Shape Memory Polymers, Adv. Mater. 31 (2019) 1805615.

[29] B.H. Kim, F. Liu, Y. Yu, H. Jang, Z. Xie, K. Li, J. Lee, J.Y. Jeong, A. Ryu, Y. Lee, D.H. Kim, X. Wang, K. Lee, J.Y. Lee, S.M. Won, N. Oh, J. Kim, J.Y. Kim, S.-J. Jeong, K.-I. Jang, S. Lee, Y. Huang, Y. Zhang, J.A. Rogers, Mechanically Guided Post-Assembly of 3D Electronic Systems, Adv. Funct. Mater. 28 (2018) 1870344.

[30] W. Lee, Y. Liu, Y. Lee, B.K. Sharma, S.M. Shinde, S.D. Kim, K. Nan, Z. Yan, M. Han, Y. Huang, Y. Zhang, J.-H. Ahn, J.A. Rogers, Two-dimensional materials in functional three-dimensional architectures with applications in photodetection and imaging, Nat. Commun. 9 (2018) 1417.

[31] H. Deng, X. Xu, C. Zhang, J.-W. Su, G. Huang, J. Lin, Deterministic Self-Morphing of Soft-Stiff Hybridized Polymeric Films for Acoustic Metamaterials, ACS. Appl. Mater. Interfaces 12 (2020) 13378–13385.

[32] C. Zhang, H. Deng, Y. Xie, C. Zhang, J.-W. Su, J. Lin, Stimulus Responsive 3D Assembly for Spatially Resolved Bifunctional Sensors, Small 15 (2019) 1904224.

[33] H.S. Jang, S. Yoo, S.H. Kang, J. Park, G.-G. Kim, H.C. Ko, Automatic Transformation of Membrane-Type Electronic Devices into Complex 3D Structures via Extrusion Shear Printing and Thermal Relaxation of Acrylonitrile–Butadiene–Styrene Frameworks, Adv. Funct. Mater. 30 (2020) 1907384.

[34] D.-Y. Khang, H. Jiang, Y. Huang, J.A. Rogers, A Stretchable Form of Single-Crystal Silicon for High-Performance Electronics on Rubber Substrates, Science 311 (2006) 208–212.

[35] D.-H. Kim, J.-H. Ahn, W.M. Choi, H.-S. Kim, T.-H. Kim, J. Song, Y.Y. Huang, Z. Liu, C. Lu, J.A. Rogers, Stretchable and Foldable Silicon Integrated Circuits, Science 320 (2008) 507–511.

[36] S.J.P. Callens, A.A. Zadpoor, From flat sheets to curved geometries: Origami and kirigami approaches, Materials Today 21 (2018) 241–264.

[37] C. Zarna, S. Rodríguez-Fabià, A.T. Echtermeyer, G. Chinga-Carrasco, Preparation and characterization of biocomposites containing thermomechanical pulp fibres, poly(lactic acid) and poly(butylene-adipate-terephthalate) or poly (hydroxyalkanoates) for 3D and 4D printing, Addit. Manuf. 59 (2022) 103166.

[38] J.W. Boleya, W.M. van Reesb, C. Lissandrelloe, M.N. Horensteinf, R.L. Trubyb, A. Kotikianb, J.A. Lewis, L. Mahadevan, Shape-shifting structured lattices via multimaterial 4D printing, PNAS 116 (2019) 20856–20862.

[39] J. Vaicekauskaite, P. Mazurek, S. Vudayagiri, A.L. Skov, Mapping the mechanical and electrical properties of commercial silicone elastomer formulations for stretchable transducers, J. Mater. Chem. C 8 (2020) 1273–1279.

[40] I.D. Johnston, D.K. McCluskey, C.K.L. Tan, M.C. Tracey, Mechanical characterization of bulk Sylgard 184 for microfluidics and microengineering, J. Micromech. Microeng. 24 (2014) 035017.

[41] Smooth-On Inc., Ecoflex 00-30 Product Data Sheet. https://www.smooth-on.com/products/ecoflex-00-30/ (accessed 25 September 2022).

[42] R.W. Ogden, Large deformation isotropic elasticity - On the correlation of theory and experiment for incompressible rubberlike solids, Proc. R. Soc. Lond. A. 326 (1972) 565–584.

[43] J.M. Burkstrand, Electron spectroscopic study of oxygen plasma treated polymer surfaces, J. Vac. Sci. Technol. 15 (1978) 223–226.

[44] L. Tang, N.Y. Lee, A facile route for irreversible bonding of plastic-PDMS hybrid microdevices at room temperature, Lab. Chip 10 (2010) 1274–1280.

[45] P.M. Dietrich, S. Glamsch, C. Ehlert, A. Lippitz, N. Kulak, W.E.S. Unger, Synchrotron-radiation XPS analysis of ultra-thin silane films: Specifying the organic silicon, Appl. Surf. Sci. 363 (2016) 406–411.

[46] R. Dahiyaa, G. Gottardib, N. Laidani, PDMS residues-free micro/macrostructures on flexible substrates, Microelectron. Eng. 136 (2015) 57–62.

[47] A.Y. Fadeev, Y.V. Kazakevich, Covalently Attached Monolayers of Oligo (dimethylsiloxane)s on Silica: A Siloxane Chemistry Approach for Surface Modification, Langmuir 18 (2002) 2665–2672.

[48] MatWeb: Material Property Data, LG Chemical HI-121H ABS, High Impact, High Whiteness.https://www.matweb.com/search/datasheettext.aspx?matid=51008 (accessed 7 June 2022).

[49] T.-I. Lee, M.S. Kim, T.-S. Kim, Contact-free thermal expansion measurement of very soft elastomers using digital image correlation, Polym. Test. 51 (2016) 181–189.